Materials Advances

ROYAL SOCIETY OF CHEMISTRY

PAPER

View Article Online
View Journal | View Issue

Cite this: *Mater. Adv.*, 2025, 6, 4115

Ionic liquid-assisted hydrothermal valorization and redox site engineering of spruce cone biowaste for high-performance heteroatom-doped and ceria-modified electrodes for sustainable supercapacitor applications†

Khadija Chaudhary, [ab] Adeen Ilyas, [c] Tomáš Zelenka, [a] Hidetsugu Shiozawa, [bd] Muhammad Farooq Warsi, [e] Eric W. Cochran *[c] and Sonia Zulfiqar *[af]

Utilizing biowaste to generate precious carbon-based electrodes offers a sustainable and cost-effective approach to advanced energy storage technologies while addressing environmental and waste management issues. In contrast to dry pyrolysis, ionic liquid-assisted hydrothermal carbonization of biomass to produce functional carbon materials has garnered significant attention due to the catalytic carbonization effects and simultaneous tuning of carbon chemistry by the inorganic salt. Herein, we report the carbonization of spruce cone biowaste in the presence of an ionic liquid *i.e.*, 1-butyl-3-methylimidazolium tetrachloroferrate ([Bmim][$FeCl_4$]). The obtained nanospheres of hydrochar were further heat-treated and modified with ceria (CeO_2) (denoted as Ce-IHSC-*x*). Experimental results showed the post-heat treatment increased the degree of graphenization and specific surface area (SSA) of hydrochar, while ceria nanoparticles along with contributing to redox active sites, help to preserve the mesoporosity in hydrochar materials. Simultaneously, $[Bmim]^+$ and $[FeCl_4]^-$ ions from ionic liquids induced Fe and N-species in the hydrochar matrix during the carbonization process, further enhancing the functionality of hydrochar. The Ce-IHSC-*x* materials exhibited a synergistic combination of high SSA, a well-tuned meso- and microporous structure, and a nitrogen-doped conductive interface. This unique architecture enabled efficient multi-dimensional ion and electron transport during charge–discharge processes. As a result, the optimized Ce-IHSC-*x* electrode demonstrated a high specific capacitance of 992.7 F g^{-1} at 0.5 A g^{-1} and 752.7 F g^{-1} at 9 A g^{-1}, outperforming many biomass-derived carbon materials. In addition, Ce-IHSC-*x* adhered good tolerance to long-term cycling with 98.8% and 95.2% retention of coulombic efficiency and specific capacitance after 7000 GCD cycles. This work further highlights the versatility of this carbonization approach combined with redox-active modification, showcasing its effectiveness in enhancing the electrochemical performance of biomass-derived supercapacitor electrodes.

Received 10th January 2025,
Accepted 6th May 2025

DOI: 10.1039/d5ma00027k

rsc.li/materials-advances

1. Introduction

Currently, the world's primary global concerns revolve around the urgent need to transition from traditional fossil fuels to alternate energy sources to address both the high energy demand and environmental pollution.[1,2] Consequently, green energy and advanced energy storage devices are considered crucial components of sustainable energy solutions for future generations. Supercapacitors have garnered significant attention from researchers among energy storage devices due to their unique characteristics including fast charging–discharging rates, long cyclic life, high power density, and enhanced safety. In principle, based on the energy storage mechanisms,

[a] *Department of Chemistry, Faculty of Science, University of Ostrava, 30. Dubna 22, Ostrava, 701 03, Czech Republic*
[b] *J. Heyrovsky Institute of Physical Chemistry, Czech Academy of Sciences, Dolejskova 3, 182 23 Prague 8, Czech Republic*
[c] *Department of Chemical and Biological Engineering, Iowa State University, Sweeney Hall, 618 Bissell Road, Ames, Iowa 50011, USA. E-mail: ecochran@iastate.edu*
[d] *Faculty of Physics, University of Vienna, Boltzmanngasse 5, 1090 Vienna, Austria*
[e] *Institute of Chemistry, Baghdad-ul-Jadeed Campus, The Islamia University of Bahawalpur, Bahawalpur, 63100, Pakistan*
[f] *Department of Physical Sciences, Lander University, 320 Stanley Ave, Greenwood, South Carolina 29649, USA. E-mail: szulfiqar@lander.edu*

† Electronic supplementary information (ESI) available. See DOI: https://doi.org/10.1039/d5ma00027k

supercapacitor electrodes fall into two main categories. Electrical double-layer capacitor (EDLC) electrodes store charge through the development of an electrically double layer at the electrode–electrolyte interface, with their capacitance primarily depending on the electrode's surface area and porosity.[3] In contrast, pseudocapacitor electrodes store charge through fast and reversible redox reactions, where the capacitance is derived from transition metal compounds and heteroatoms such as nitrogen (N), oxygen (O), and sulfur (S).[4,5]

Biomass-derived activated biochar has gained significant attention as a new carbon source to conventional carbon materials (derived from coal, petroleum, and their derivatives[6–8]) for supercapacitor electrodes due to its low cost, high porosity/large pore volume, good electrical conductivity, and large surface areas.[9] Until the recent past, the thermochemical conversion of biomass to porous carbon materials was limited to dry pyrolysis, and/or physical and chemical activation processes at high temperatures.[10] However, the carbon material obtained through dry pyrolysis is usually flawed by low carbon yield (especially with cellulose-rich agro-wastes), limited coverage of surface functional groups, and inadequate control over textural properties.[11,12] In addition, the energy density and capacitance retention of these porous carbon materials further need to be improved by surface modification and precise regulation of pore structure.[13–15]

Lately, hydrothermal carbonization (HTC), also referred to as wet pyrolysis, has emerged as an effective strategy for converting lignocellulosic biomass into functional carbon materials under relatively mild temperatures (<250 °C) and autogenous pressure (<10 bar).[16] HTC process facilitates the transformation of biomass into functional hydrochar through a series of reactions, including dehydration, decarboxylation, polymerization, and aromatization.[11] While water is the conventional solvent in wet-pyrolysis, most recently ionic liquids (ILs) have gained increasing attention for their ability to enhance carbonization pathways and enable controlled functionalization in the resulting carbon materials. ILs or so-called designer solvents are salts that exist in liquid form at temperatures below 100 °C and consist of an organic cation and inorganic anion.[17] Due to their zero vapor pressure, excellent thermal stability, structure-directing capability, and unique ability to dissolve cellulose, lignin, and even entire lignocellulosic structures, ILs serve as promising alternative solvents to drive biomass conversion towards advanced carbonaceous materials with tailored physicochemical properties.[18] For instance, Cibien *et al.* converted cocoa bean shells into solid char using a Lewis acid ionic liquid, 1-butyl-3-methylimidazolium tetrachloroferrate ([Bmim][$FeCl_4$]) at 240 °C.[19] [$FeCl_4$]$^-$ anions were reported to stabilize carbon oxygenated functional groups that lead to enhanced carbon yield and favored generation of pores. Liu *et al.* successfully carbonized Junjun grass at 180 °C in the presence of ([Bmim][$FeCl_4$]) and subsequently activated it with KOH to obtain porous carbon materials with high surface areas.[20] Aldroubi *et al.* transformed sugarcane bagasse into various porous carbon nanostructures exhibiting different textural properties in the presence of imidazolium tetrachloroferrate ILs bearing different lengths and benzyl group in the alkyl chain of organic cation.[11] In addition, Zhang and co-workers synthesized heteroatom doped (F, B, N) carbon materials through carbonization of glucose, cellulose, and sugar cane bagasse at 200 °C using recyclable bis-methyl imidazolium type ILs with different inorganic anions ([BF_4^-] and [Tf_2N^-]).[21] In these reports authors highlighted multifunctional roles of ILs, acting as: (i) Lewis acid catalyst for carbonization, (ii) porogen, and (iii) heteroatom source. Moreover, functional hydrochars prepared *via* HTC demonstrated superior performance as electrodes for oxygen reduction reaction,[21,22] lithium-ion batteries,[23] and supercapacitors.[20]

That being said, the carbonization of biomass in presence of ILs remains an emerging area of research with reaction mechanisms still requiring further understanding, and a range of carbon precursors/ILs systems yet need to be explored. In this study, we employed an ionic liquid-rich hydrothermal carbonization process integrated with post-heat treatment to enhance the properties of spruce cone-derived lignocellulosic biomass. This wet-pyrolysis process was conducted in presence of [Bmim][$FeCl_4$] IL, which played a pivotal role in facilitating the biomass conversion and impacting desirable structural and functional characteristics of resulting materials. Norway spruce (Picea abies L. H. Karst.), a widely distributed and abundant species in Northern and Central Europe, is primarily harvested for its timber; however, its cones, produced in large quantities, are often considered a plentiful byproduct of forestry operations. The conversion of spruce cones (SC) into valuable products will aid in waste management while promoting the development of a local circular bioeconomy. What's more, a step further, ceria (cerium dioxide/CeO_2) was incorporated into synthesized hydrochar because of the advantageous redox properties of cerium (Ce), which stem from its specific 4f configuration as well as its status of most abundant rare earth metal.[24,25] [Bmim][$FeCl_4$] was found to induce the formation of unique nanometer-sized carbon spheres (34–51 nm) while integrating heteroatoms (Fe and N) in the hydrochar matrix. The post-heat treatment further improved the structural properties by improving the degree of graphenization and surface area of hydrochar. The hydrochars prepared with ceria were found to have more interesting pore structure profiles with a good balance of micro- and mesoporosity, required for enhanced electrochemical properties. Eventually, the optimized hydrochar (Ce-IHSC-900) showed high specific capacitance (992.7 F g^{-1}), rate capability (75.8%), and cyclic stability (95.2%), suggesting spruce cone-derived and ceria modified hydrochar as attractive functionalized carbon material for further electrochemical applications.

2. Experimental section

2.1. Chemical reagents

1-Butyl-3-methylimidazolium chloride ([Bmim][Cl], $C_8H_{15}ClN_2$); $\geq$98.0%, cerium(III) nitrate hexahydrate $Ce(NO_3)_3{\cdot}6H_2O$; 99%, iron(III) chloride hexahydrate $FeCl_3{\cdot}6H_2O$; 97%, Potassium hydroxide (KOH); 90%, were procured from Merck. Spruce cones were obtained from a local garden in Ostrava, Czech Republic.

2.2. Synthesis of [Bmim][$FeCl_4$]

For the preparation of IL, equal moles of [Bmim][Cl] (14.6 g) and $FeCl_3 \cdot 6H_2O$ (23.1 g) were mixed in 50 mL beaker. The mixture was stirred in the solid state at room temperature for 30 min, forming a solution. This solution was left undisturbed overnight, leading to the separation into two immiscible layers: an upper aqueous layer and a bottom layer consisting of [Bmim][$FeCl_4$] IL. The upper aqueous layer was carefully separated using a pasteur pipette, and the bottom dark brown phase was heated at 60 °C overnight to remove residual water from the [Bmim][$FeCl_4$] IL.

2.3. Synthesis of hydrochar

For the preparation of hydrochar, spruce cones were initially washed thoroughly with tap water to remove any loose dust particles, followed by rinsing with deionized water to eliminate soluble impurities. The cleaned cones were then dried at 100 °C for 12 h to ensure complete moisture removal. After drying, the scales were separated from the cones, ground using a M 20 Universal Mill (IKA Mills), and sieved granulometrically using a laboratory test sieve (Prufsieb DIN 1171, 1.0 mm), ensuring that the particles were $\leq$1 mm in size for further processing.

For hydrothermal carbonization (HTC), 4 g of well-ground spruce cone powder was dispersed in 30 mL of distilled water and stirred for 10 min. 10 mL of [Bmim][$FeCl_4$] was added to it and stirring was continued for further 20 min. The mixture was transferred to 50 mL autoclave and incubated at 220 °C for 12 h. Next, the carbonized biomass (hydrochar) was removed from the autoclave, filtered, and dried at 70 °C. For comparison, pure hydrochar without the addition of IL was also prepared following the same methodology and experimental conditions.

2.4. Preparation of Ce-IHSC-*x*

In a typical synthesis, 1.5 g of hydrochar was added in 40 mL of 0.1 M $Ce(NO_3)_3$ solution and stirred for 20 min. To adjust the pH to 10, 1 mL of 2 M KOH solution was gradually added to the stirring mixture. The solution was then stirred continuously at room temperature for 12 h. Following this, the product was thoroughly washed with deionized water to remove unreacted reagents and dried at 70 °C overnight. The dried material was then heat-treated in a tube furnace under a nitrogen (N_2) atmosphere at 700 °C, 800 °C, and 900 °C for 2 h, with the temperature ramped at a controlled rate of 5 °C min^{-1}. Resulting ceria-modified, heteroatom-doped hydrochar samples derived from the ionic liquid-assisted hydrothermal carbonization of the spruce cone were labeled as Ce-IHSC-*x*, where *x* denotes the specific post-heat treatment temperature.

For comparison of electrochemical performance in absence of IL, ceria-modified hydrochar without IL was also prepared using the same methodology described above, with the omission of [Bmim][$FeCl_4$] in section 2.3, and was then heat-treated at 900 °C.

2.5. Materials characterization

Different physicochemical characterizations were carried out to confirm the synthesis and study the properties of prepared materials. Phase study was done on Siemens D 500 diffractometer using copper Kα X-ray radiation source (Wavelength = 1.5432 Å) operated at a power of 45 kV. Chemical bonding information was gathered through Raman and Fourier transform infrared (FT-IR) spectroscopy measurements on LabRAM HORIBA Jobin-Yvon (laser = 633 nm) and NICOLET 6700 FT-IR instruments, respectively. For Raman curve fitting, origin software was used to fit the data using a combination of Lorentzian and Gaussian functions.[26] Initial band positions were determined by peak assignments from literature and our experimental data. Morphological and elemental analyses were performed on Hitachi SU4800 field emission scanning electron microscope (FESEM). Textural or particle size analysis was carried out on Bruker dimension icon atomic force microscope (AFM) operating in tapping mode. For AFM analysis, prepared samples were dispersed in isopropyl alcohol and deposited on SiO_2 substrate. The chemical structure of prepared hydrochars was determined by X-ray photoelectron spectroscopy (XPS) using the Kratos Amicus/ESCA 3400 instrument. XPS spectra were fitted using Gaussian function, allowing the FWHM of the peak to remain unconstrained during the fitting process. Thermogravimeter STA449F1 (Netzsch) was used for the thermal analysis of hydrochar under an oxidizing atmosphere comprised of 20% oxygen and 80% argon. Surface area and pore size measurements were accomplished on the Quantachrome Instruments gas sorption analyzer. From N_2/77K adsorption isotherms, BET area was calculated according to Rouquerol's consistency criteria.[27] Pore size distributions were determined using adsorption branch through hybrid QSDFT adsorption kernel, assuming slit-shaped micropores and cylindrical mesopores. Micropore and mesopore volumes and areas were derived by integrating the pore size distribution curves within the specified pore size range. Hydrochars were degassed at 200 °C for 16 h under the vacuum before analysis. Electrolyte wettability for the prepared hydrochar samples was analyzed by the contact angle measurements on Ossila contact angle goniometer. For contact angle measurements, the electrode slurry was prepared following the method outlined in Section 2.6 and uniformly deposited onto a glass substrate.

2.6. Electrochemical measurements

All the electrochemical studies were conducted on GAMRY interface 1000E Potentiostat. To prepare a working electrode, 5 mg of functionalized hydrochar was dispersed in ethanol and the mixture was ultrasonicated for 2 to 3 min to prepare a homogeneous electrode slurry. Electrode slurry was then drop cast on Ni foam (1 × 1 cm^2) followed by drying at 60 °C. The prepared electrode was integrated into a three-electrode assembly, with a platinum-wire as a counter electrode, and silver/silver chloride as a reference electrode. To evaluate the supercapacitor performance, different electrochemical tests *i.e.*, cyclic voltammetry (CV, 5–100 mV s^{-1}), galvanostatic charge–discharge (CD, 0.5–9 A g^{-1}), and electrochemical impedance spectroscopy (EIS, 1 to 100 kHz) were carried in 2 M KOH electrolyte.

3. Results and discussion

Ceria modified hetero atom doped hydrochar materials donated as Ce-IHSC-*x* were prepared by the ionic liquid-assisted

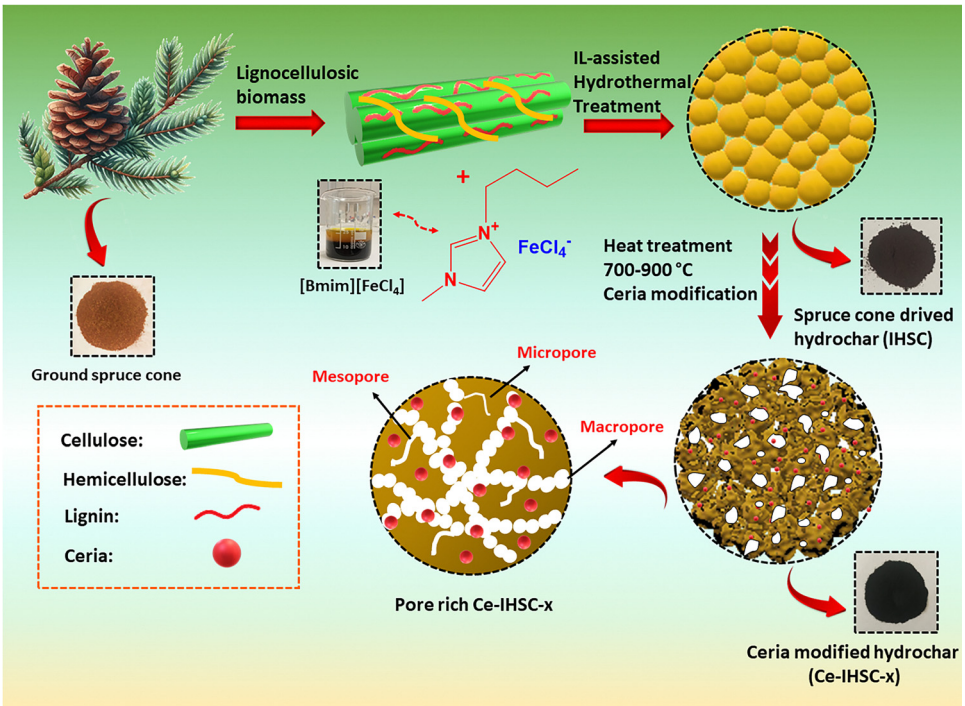

Fig. 1 Schematic illustration for the synthesis of ceria-modified spruce cone-derived hydrochar.

hydrothermal carbonization of the spruce cone as illustrated in Fig. 1. [Bmim][$FeCl_4$] IL prepared by a simple organic reaction, not only provide the reaction medium for carbonization of lignocellulosic biomass but also acted as a source of N and Fe- species. During the HTC at 220 °C in the presence of [Bmim][$FeCl_4$], the carbonization process is accompanied by various intramolecular reactions (condensation, dehydration, and decarbonylation) which resulted in the generation of polyaromatic domains.[23] Following HTC, hydrochar undergoes further carbonization during the post-heat treatment and generates volatile species (hydrocarbons (C_xH_y), oxygenated hydrocarbon ($C_xH_yO_z$), CO, and H_2O) which at high temperature react with $[FeCl_4]^-$ to produce some low valence Fe species. These Fe species can act as catalyst to promote the graphenization of hydrochar.[22] Meanwhile, the cationic part of ionic liquid was decomposed to induce N as a heteroatom in the resulting carbon framework.[28]

3.1. XRD analysis

The phase composition and crystalline structure of hydrochar samples were analyzed by XRD. XRD patterns of IHSC and IHSC-900 in Fig. 2(a) exhibit two broad peaks at ~24.8° and ~43.4° corresponding to the (002) and (100) planes of turbostratic carbon, respectively. According to Bragg's law ($n\lambda = 2d\sin\theta$) the value of d_{002}-mean interlayer spacing for the prepared hydrochars is around 0.357 nm, slightly higher than that of graphite (0.335 nm), which indicates the presence of disordered carbon domains and larger interlayer spacing. It is noteworthy that, in addition to the (002) plane, the XRD pattern of pure hydrochar in Fig. S1 (ESI†) exhibits two additional peaks at 18.8° (110) and 39.4° (040), which are indicative of the crystalline structure of raw cellulose.[29] This cellulose crystallinity contributes to a relatively sharper (002) peak in pure hydrochar. The presence of these peaks indicates incomplete carbonization in pure hydrochar, in contrast to IHSC, where Fe-containing IL effectively catalyzes the carbonization process due to superior solvation properties and better solubility of cellulosic components than water.[22] Additionally, the appearance of new, less intense peaks (highlighted in Fig. S2, ESI†) in the IHSC-900 after the post heat treatment, is attributed to the formation of Fe-species, such as $FeCO_3$ and Fe_3C, within the carbon matrix.[30,31] According to Xie *et al.*, these Fe-species are generated through the high-temperature carbothermal reduction of the IL entrapped within the carbon framework during the synthesis process.[32] Alternatively, multiple sharp peaks were observed in the XRD patterns of Ce-IHSC-700, Ce-IHSC-800, and Ce-IHSC-900 in Fig. 2(a). These peaks at 28.5°, 33°, 47.4°, 56.1°, 59°, and 69.5° correspond to (111), (200), (220), (311), (222), and (400) reflections of cubic CeO_2 (standard JCPDS# 34-0394). The XRD patterns of all ceria-modified hydrochar samples show the same characteristic peaks for CeO_2. Nevertheless, the intense CeO_2 peaks obscure the (002) and (001) carbon reflections in XRD patterns of Ce-IHSC-*x*. The crystallite sizes (D) of CeO_2 in the hydrochars with different post-heat treatment temperature were evaluated by Scherrer formula given in the following equation:

$$D = k\lambda/(\beta \times \cos\theta) \quad (1)$$

In above equation, λ represents the wavelength of the X-ray source, β denotes the full width at half maximum (FWHM) of the diffraction peak, k is the dimensionless Scherrer constant,

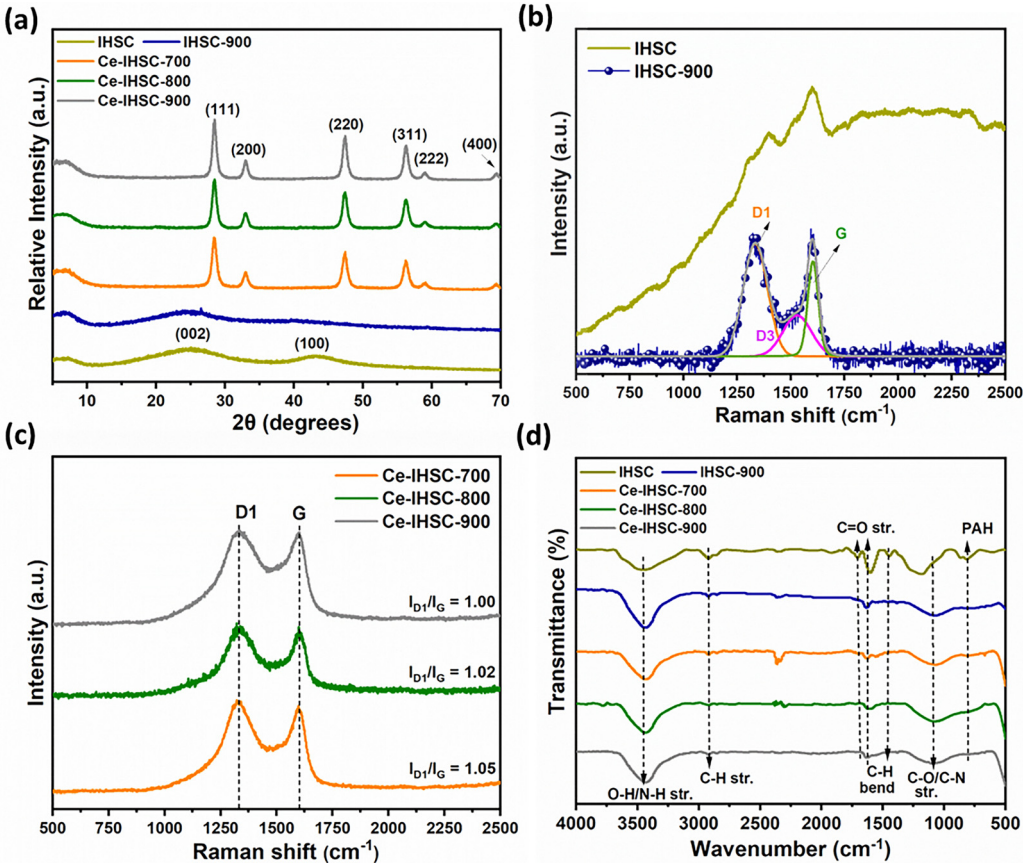

Fig. 2 (a) XRD patterns of IHSC, IHSC-900, and Ce-IHSC-*x*, (b) Raman spectra of IHSC, IHSC-900, (c) Raman spectra of Ce-IHSC-*x*, and FT-IR spectra of IHSC, IHSC-900, and Ce-IHSC-*x*.

and θ is the Bragg diffraction angle. The average crystallite sizes of Ce-IHSC-700, Ce-IHSC-800, and Ce-IHSC-900 were calculated as 8.2, 9.4, and 10.3 nm, respectively. The increase in crystallite sizes of CeO_2 with the increase in temperature may be caused by the Ostwald ripening and/or reduction in structural defects such as lattice strain and grain boundaries at the higher temperature, which leads to the formation of larger and well-ordered crystallites.

3.2. Raman analysis

To get insight of the structural order of prepared hydrochar samples, Raman spectra were recorded using 633 nm laser. All hydrochar samples in Fig. S3 (ESI†) and Fig. 2(b and c) exhibit two common characteristic bands in all the Raman spectra: the D1-band around 1350 cm^{-1} is accompanied by the breathing mode of six-membered carbon rings, which indicates structural defects within the sp^2-carbon network, whereas the G-band around 1600 cm^{-1} relates to the in-plane vibrational mode of sp^2-hybridized carbon atoms in graphenic/graphitic domains. In addition to D and G bands, Fig. S3 (ESI†) exhibit several small bands in range of 150–1000 cm^{-1} in pure hydrochar which arise from the raw cellulose.[33] Noticeably, IHSC in Fig. 2(b) displays strong fluorescence that led to the deviation of baseline. This phenomenon can be accredited to the presence of auxochromic groups in the polyfuranic aromatic structure coming from the thermochemical degradation of cellulose in IHSC.[34] For IHSC-900, fluorescence diminishes and a significant shift in D1-band is observed as compared to IHSC, due to the formation of new stable defects at high temperatures and bond relaxation in defective regions.[35] The Raman spectra of IHSC-900 and Ce-IHSC-*x* can be further resolved to get another disorder-induced D3 band at 1525 cm^{-1} (indicated by deconvolution of IHSC-900 in Fig. 2(b)).[36] The D3 is also ascribed to an amorphous carbon phase and may arise in hydrochars due to the formation of higher-order defects or multi-phonon scattering interactions.[37] Meanwhile, the D1-band to G-band ratio (I_{D1}/I_G) for Ce-IHSC-700, Ce-IHSC-800, and Ce-IHSC-900 is calculated as 1.05, 1.02, and 1, respectively. This decrease in I_{D1}/I_G ratio with an increase in temperature suggests a reduction in overall defects concentration and improvement in the structural order of carbon following high-temperature carbonization.

3.3. FT-IR analysis

Fig. 2(d) display FT-IR spectra of IHSC, IHSC-900, Ce-IHSC-700, Ce-IHSC-800, and Ce-IHSC-900. The characteristic band at ~3118–3693 cm^{-1} in all hydrochar samples can be assigned to the O–H/N–H stretching vibrations. Two small bands observed at ~2858 cm^{-1} and ~2923 cm^{-1} are due to stretching modes of C–H bond in aliphatic CH_2 and CH_3. The decrease in

intensity of the bands associated with these alkyl groups in IHSC-900 and Ce-IHSC-*x* samples at higher carbonization temperatures suggests that these groups undergo thermal decomposition or cracking, leading to their loss or transformation into other functional groups.[38] The bands at 1617 cm^{-1} and 1700 cm^{-1} are associated with C═O stretching modes in the aliphatic compounds and aromatic ring, respectively. Meanwhile, a band at 1463 cm^{-1} indicates aliphatic C–H bending. The broad band at 1081 cm^{-1} is related to the C–O/C–N stretching bonds. Moreover, bands observed at 829 cm^{-1} and 853 cm^{-1} could be linked to the existence of polyaromatic hydrocarbons which are generated during the pyrolysis of biomass.[39] Overall, the trend in the FT-IR spectra is consistent with previous findings by Chen *et al.* for alfalfa biochar, where the intensity of the oxygen-containing functional group decreased after the heat treatment.[40]

3.4. Morphological and elemental analyses

The morphology or microstructure of prepared hydrochar was characterized by the FESEM analysis. Representative FESEM images of the hydrochar samples are presented in Fig. 3 at different magnifications. Fig. 3(a and b) illustrates that the HTC of SC at 220 °C in the presence of [Bmim][$FeCl_4$] resulted in the formation of well-defined carbon spheres. The morphology of pure IHSC nanospheres appears uniform across the entire IHSC sample. However, heat treatment at 900 °C induced significant morphological changes, as illustrated in Fig. 3(c–f). The IHSC-900 and Ce-IHSC-900 samples demonstrate partial coalescence, leading to the formation of crannies or macropores. These features can be attributed to the combustion of residual organic matter and the evolution of gases during the heat treatment process. The heat-treated hydrochar samples depicted in Fig. 3(c–f) exhibit a generally rough and amorphous texture. Notably, compared to IHSC-900 (Fig. 3(c)), the Ce-IHSC-900 sample (Fig. 3(e)) displays a more open and porous microstructure, characterized by large interconnected voids among the carbon nanoparticles. This transformation in morphology or packing density is likely a result of interactions between ceria and carbon nanoparticles. These interactions mitigate excessive particle aggregation and facilitate the development of a more open, pore-rich network. The high degree of interstitial porosity observed in Ce-IHSC-900 suggests that it will provide a three-dimensional network of interconnected pathways, facilitating the transport of ions and electrons within the carbon matrix during the electrochemical process. The 2D and 3D AFM images of IHSC, IHSC-900, and Ce-IHSC-900 are shown in Fig. 4(a–f), which align well with the observation made by SEM analysis. The average particle heights of segregated spherical particles for IHSC were found to be in the range of 3–5 nm. Whereas AFM images of IHSC-900 and Ce-IHSC-900 showed particle's heights in range of 18–27 and 2–10 nm, respectively. The overall smaller particle sizes of Ce-IHSC-900 as compared to IHSC-900 reaffirms that the addition of ceria inhibited particle growth possibly by preventing sintering or stabilizing smaller particles. In addition, the EDX spectrum of Ce-IHSC-900 in Fig. S4 (ESI†) indicates the co-existence of all elements *i.e.*, C, O, N, Ce, Fe, and Cl. The wt% of all elements of prepared hydrochars are presented in Table S1 (ESI†). Discernibly, there is a steady increase in C, N, and Fe content with rising temperature, which can be attributed to the enhanced degree of graphenization and the more effective integration of IL components into the hydrochar at elevated temperatures.

3.5. XPS analysis

The chemical bonding and chemical composition of biochar was studied through XPS analysis. Fig. 5(a–e) depicts the deconvoluted XPS spectra of Ce-IHSC-900 corresponding to C 1s, N 1s, Fe 2p, Ce 3d, and O 1s. As shown in Fig. 5(a), the C 1s XPS spectrum was fit into four peaks corresponding to carbide C, graphitic C, C–N/C–O, and C═O functional groups at binding energies of 283.6, 284.6, 285.7, and 288.2 eV, respectively.[41,42] The deconvoluted N 1s spectrum in Fig. 5(b) reveals the existence of pyridinic, pyrrolic, pyrindonic, and graphitic N at 398.2, 399.5, 400.5, and 402.2 eV, respectively.[43,44] According to a previous report on the HTC of sawdust, pyridinic and pyrrolic nitrogen are prevalent species in the hydrochar. However, high-temperature carbonization and

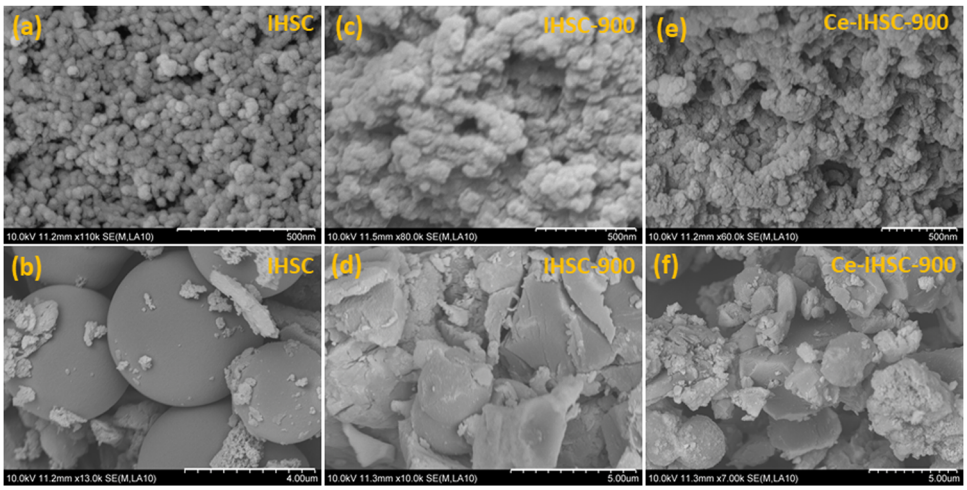

Fig. 3 FESEM images of (a) and (b) IHSC, (c) and (d) IHSC-900, and (e) and (f) Ce-IHSC-900.

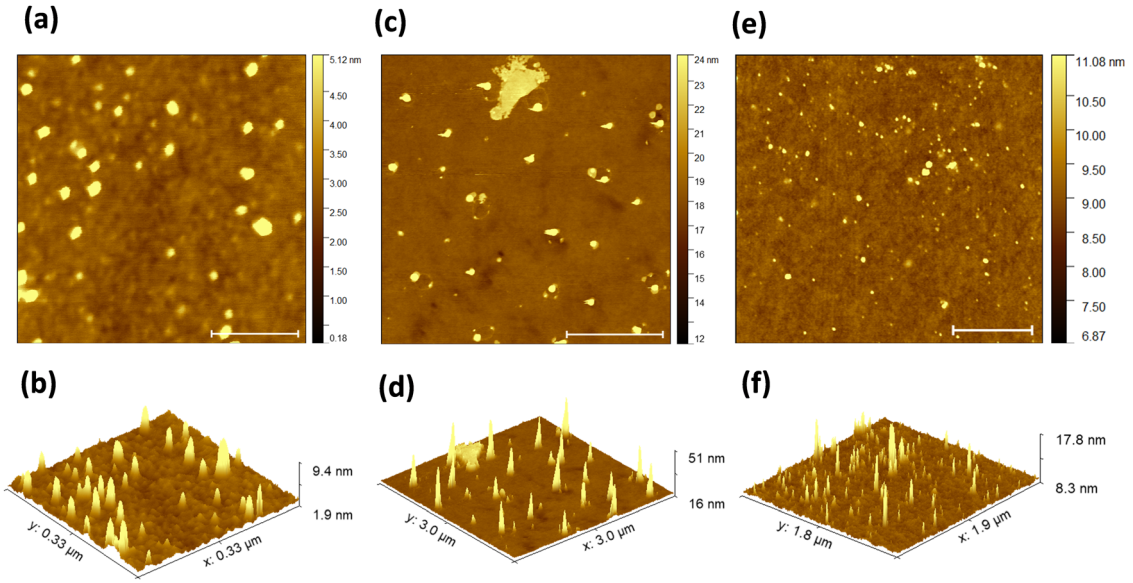

Fig. 4 2D and 3D AFM images of (a) and (b) IHSC, (c) and (d) IHSC-900, and (e) and (f) Ce-IHSC-900.

catalysis by Fe species transform some of these nitrogen species into graphitic nitrogen.[28] The deconvolution of the Fe 2p XPS spectrum in Fig. 5(c) showed five peaks associated with Fe–C, Fe^{2+} (710 and 723.9 eV), and Fe^{3+} (712 and 727.8 eV) indicating the formation of Fe_3C and presence of other Fe species in the hydrochar.[45] Fig. 5(d) displays the Ce 3d spectrum, which fits into six peaks. The spin splitting peaks located at 882.9, 886.3, 898.6, 901, 906.1, and 917.4 eV belong to Ce $3d_{5/2}$ and Ce $3d_{3/2}$ of Ce^{4+} and Ce^{3+} oxidation states in CeO_2.[46] The peak fitting for O 1s in Fig. 5(e) shows three distinct peaks at 529.7, 530.9, and 532.4 eV, corresponding to a doublet of lattice oxygen (O_L) for Ce^{4+}, Ce^{3+}, and oxygen vacancy (O_V), respectively.[46]

3.6. BET analysis

To quantitatively investigate the effect of internal structure and porous characteristics of hydrochars on the electrochemical performance, N_2 adsorption–desorption analysis was carried out at 77 K. The N_2 adsorption–desorption isotherms for all hydrochar samples are presented in Fig. S5(a) (ESI†) and Fig. 6(a). As shown, pure hydrochar and IHSC exhibit a type II isotherm with an H3-hysteresis loop at elevated relative pressure, indicating the presence of meso and macropores. In contrast, adsorption features of IHSC-900 and Ce-IHSC-*x* reveal type I/II isotherm behavior with a narrow H4-hysteresis loop at medium and high pressures, indicating a high abundance of micropores and some mesopores (because of the H4-hysteresis loop). Strong low-pressure adsorption in IHSC-900 and Ce-IHSC-*x* indicates the generation of micropores in hydrochars at high post-heat treatment temperatures due to the decomposition of organic matter into small molecules and the release of volatiles. Further, the slight increase in the adsorption in isotherms at high P/P_0 (~0.9–1.0) suggests capillary condensation, likely due to interparticle voids or macropores, as observed in SEM.[19] The pore size distribution (PSD) curves (<2–33 nm) in Fig. S5(b) (ESI†) and Fig. 6(b) indicate a predominance of mesoporosity in pure hydrochar and IHSC. Noticeably, IHSC exhibited a PSD in the ~3.5–33 nm range, whereas pure hydrochar showed comparatively broad mesopores in the range of ~7–33 nm, with peak pore diameters lying at ~4.5 and ~13.3 nm, respectively. The difference in mesopore sizes likely originate due to different carbonization mechanisms. In pure HTC, hydrothermal water interacts with biopolymers *via* H-bonding and hydrolysis, promoting structural decomposition and larger mesopores. On the contrary, as described by Xie *et al.* [Bmim][$FeCl_4$] might closely interact with biopolymers, not only by H-bonds but also through π-interactions of the imidazolium ring, facilitating nucleation of small particles and restricting the mesopore growth.[32] Similarly, post heat-treated hydrochar (IHSC-900) is dominated by micropores (~0.6–0.8 nm), while Ce-IHSC-*x* features a combination of micropore (~0.6–2 nm) and mesopores (~2–10 nm). A close view of micropore sizes distribution in prepared hydrochars is provided in Fig. S6 (ESI†). Further, a detailed summary of studied textural characteristics is provided in Table 1. The BET area for pure hydrochar, IHSC, IHSC-900, Ce-IHSC-700, Ce-IHSC-800, and Ce-IHSC-900 is obtained as 46, 82, 632, 562, 455, and 465 $m^2\ g^{-1}$, respectively. The results in Table 1 indicate that the introduction of ceria reduced the surface area to some extent, however it somehow promotes the generation of mesopores in Ce-IHSC-*x*. The ratio of the surface area contributed by meso- and micropores in the range of <2 to 33 nm for Ce-IHSC-700, Ce-IHSC-800, and Ce-IHSC-900 is 0.048, 0.059, and 0.098, respectively, demonstrating more mesopores in Ce-IHSC-900 as compared to former two. This data verifies that both ceria and post-heat treatment temperature play a decisive role in tailoring the textural properties of the synthesized hydrochars.

3.7. Thermogravimetric analysis

The thermal decomposition behavior of prepared hydrochar samples was studied by TG-DTG analysis in an oxidative

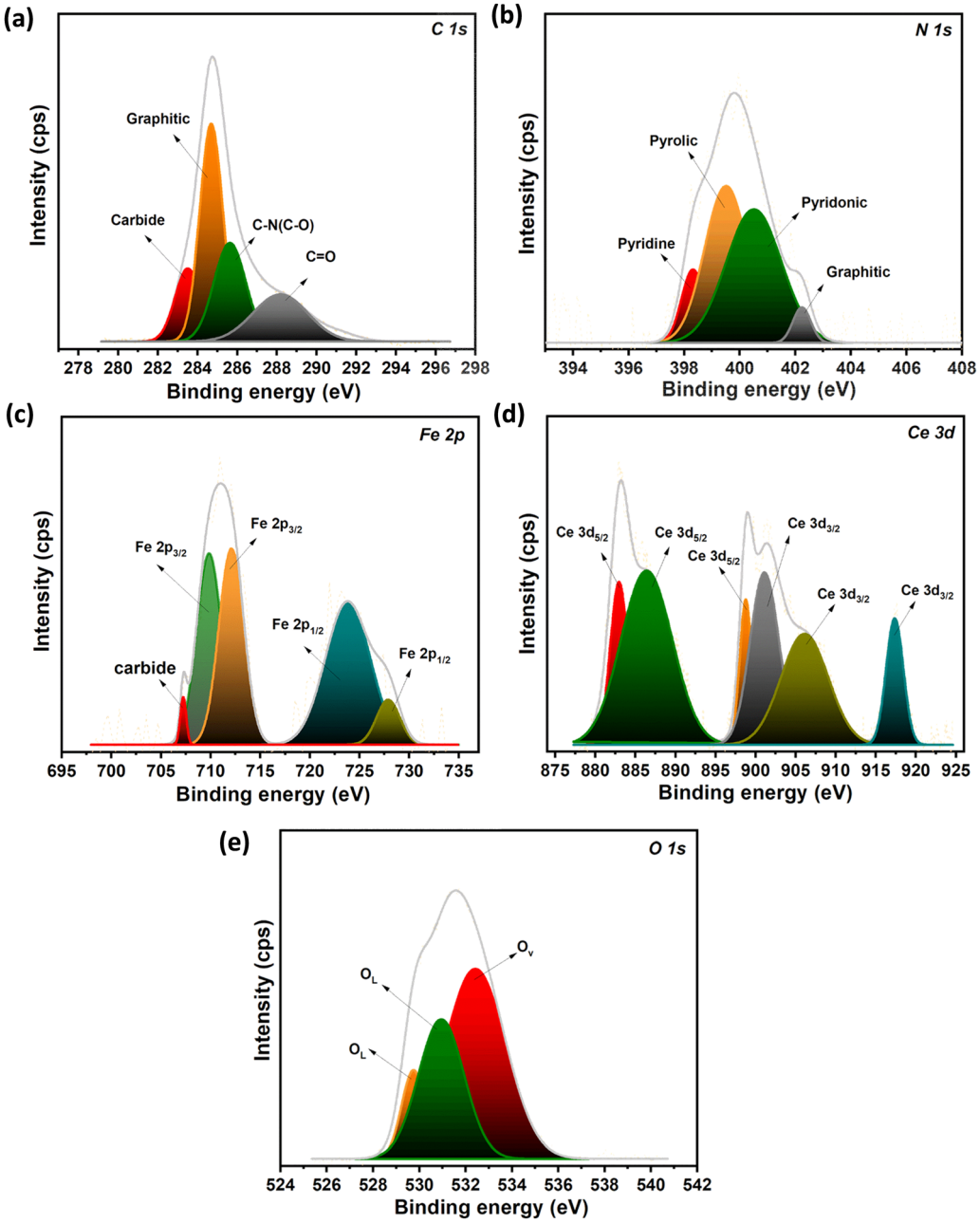

Fig. 5 Deconvulated XPS spectra of (a) C 1s, (b) N 1s, (c) Fe 2p, (d) Ce 3d, and (e) O 1s.

atmosphere at a heating rate of 10 °C min^{-1}. The combined TG % weight loss curves and DTG (min^{-1}) plots as a function of temperature are presented in Fig. 7(a–e). The total weight loss of hydrochar samples can be divided into three regions. The first region up to ~220 °C corresponds to the weight loss due to the concomitant vaporization of adsorbed moisture and low-temperature volatiles in the hydrochars. This weight loss is identified as the first peak in DTG plot. The second region is the active decomposition zone for the hydrochars which extends up to ~600 °C. As a dominant decomposition region, this section of TG-DTG is characterized by the generation of the highest number of volatiles. The weight loss in this region is mainly due to the decomposition of high molecular weight molecules *i.e.*, cellulose and hemicellulose to low molecular weight CO and CO_2. This decomposition is marked by two distinct exothermic features in the DTG plot: a prominent peak and a less intense shoulder. In addition, the gradual decomposition of lignin also starts in the active decomposition region characterized by long tailing of DTG peaks, which extends up to the third passive decomposition region. The total weight loss recorded for IHSC, IHSC-900, Ce-IHSC-700, Ce-IHSC-800, and Ce-IHSC-900 was 98.4%, 98.03%, 73.9%, 61.9%, and 61.5%, respectively. It is worth noting that although the weight loss in the case of IHSC and IHSC-900 suggests nearly complete

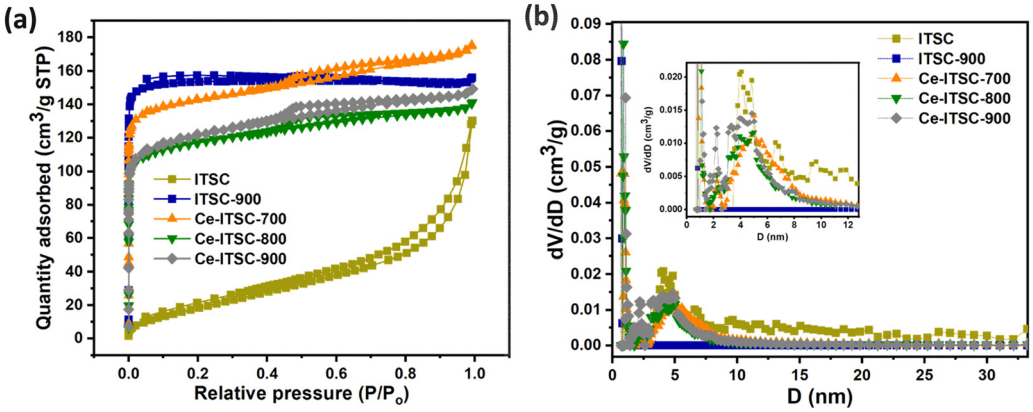

Fig. 6 (a) N_2 adsorption–desorption and (b) pore size distribution plots for IHSC, IHSC-900, and Ce-IHSC-*x* at 77 K.

Table 1 Surface characteristics of prepared hydrochars determined by N_2 adsorption–desorption experiments at 77 K

Sample	Surface area/ SA (m^2 g^{-1})	SA Micro (m^2 g^{-1}) Micro (< 2 nm)	SA Meso (m^2 g^{-1}) Meso (2–33 nm)	$SA_{Meso/Micro}$	Volume (cm^3 g^{-1}) Micro (<2–33 nm)	Volume (cm^3 g^{-1}) Meso (<2–33 nm)
Pure hydrochar	46	0.0	46	—	0.000	0.181
IHSC	82	0.0	61.7	—	0.000	0.143
IHSC-900	632	855.6	0	—	0.224	0
Ce-IHSC-700	562	760.6	37.1	0.048	0.194	0.055
Ce-IHSC-800	455	597.2	35.3	0.059	0.156	0.043
Ce-IHSC-900	465	480.0	47.3	0.098	0.153	0.055

burnout of organic matter, the small residual matter (~1.6–2%) remains in final products. This residual mass may correspond to inorganic impurities, including Fe-species detected by XRD and XPS. Nonetheless, under the oxidative conditions during TGA, Fe-species may undergo decomposition or oxidation, resulting in the formation of ultrafine iron oxide nanoparticles (FeO and Fe_2O_3).[28] These ultrafine particles can become highly dispersed, making them difficult to detect by TGA due to their small size and the low detection limits of the technique. Certainly, the hydrochar with the low post-heat treatment temperature (Ce-IHSC-700) had a higher fraction of unconverted organic volatiles and less condensed organic domains which decompose and oxidize readily under oxidative conditions. Whereas, the higher post-heat treatment temperature induced extensive carbonization and condensed graphenic domains making Ce-IHSC-800 and Ce-IHSC-900 more resistive to oxidation and, thus, lower weight loss. Further, the difference in the % weight loss of IHSC and Ce-IHSC-*x* can be used to find the weight of ceria in the hydrochar which was identified as the pale yellow powder at the end of TG-DTG experiment.

3.8. Contact angle measurements

Contact angle measurements were conducted to evaluate the wettability of the prepared materials with the electrolyte (2 M KOH). The results, presented in Fig. S7 (ESI†) and Fig. 8, indicate that the electrolyte droplet forms a contact angle of 72.2° on IHSC, which is lower than that of pure hydrochar (91.5°), representing improved wettability. The enhanced interaction between IHSC and the electrolyte is attributed to the incorporation of hydrophilic moieties and heteroatoms from the IL, which modify the surface chemistry. However, after heat treatment at 900 °C, the contact angle of IHSC-900 increases to 99.1°, primarily due to the partial removal of polar functional groups. In contrast, the contact angles for Ce-IHSC-700, Ce-IHSC-800, and Ce-IHSC-900 are 33.7°, 37.1°, and 40°, respectively, demonstrating a gradual increase in hydrophobicity with rising heat treatment temperatures. This gradual increase in hydrophobicity is a byproduct of increased graphenization at high temperature. However, despite this increase in hydrophobicity, ceria-modified hydrochars exhibit overall improved wettability compared to IHSC-900. This enhancement is driven by the strong surface polarity introduced by CeO_2, where the presence of redox-active Ce^{3+}/Ce^{4+} species facilitates stronger electrolyte interactions, thereby promoting superior electrolyte affinity. The improved wetting behavior of Ce-IHSC-*x* facilitates faster electrolyte infiltration and improved electrochemical performance.

3.9. Supercapacitor measurements of hydrochar

Recent studies show that functionalized carbons constitute a promising class of materials for electrochemical applications. Our synthesized hydrochars were tested as the active materials for supercapacitor electrodes in a three-electrode configuration with 2 M KOH as the electrolyte solution. The electrochemical activity of hydrochars was initially examined by the cyclic voltammetry (CV) measurements. The CV profiles of pristine IHSC-900 and Ce-IHSC-*x* are displayed in Fig. 9(a) at a constant scan rate of 100 mV s^{-1}. The appearance of a broad hump at the

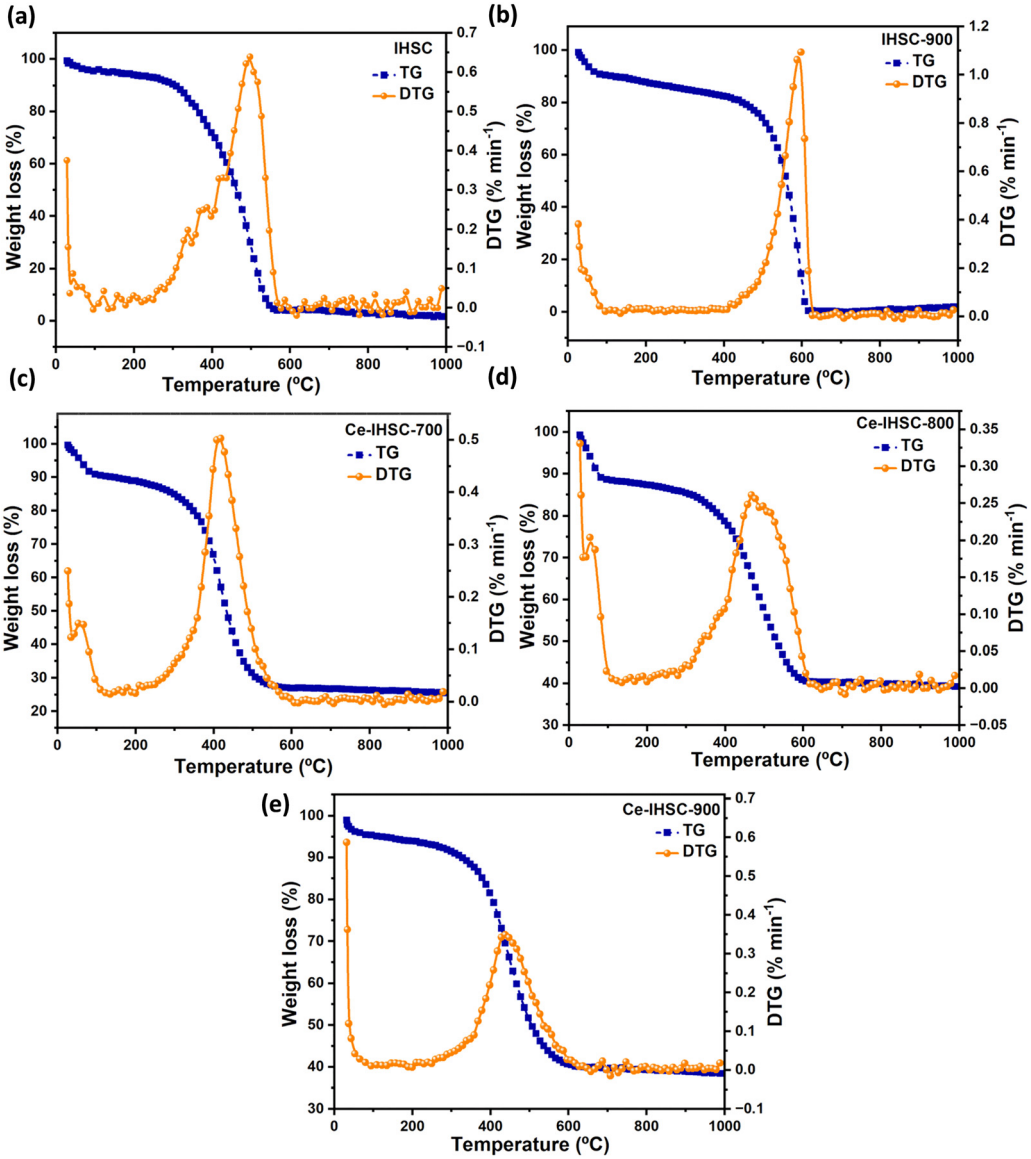

Fig. 7 TG % weight loss and DTG plots for (a) IHSC, (b) IHSC-900, and (c)–(e) Ce-IHSC-*x*.

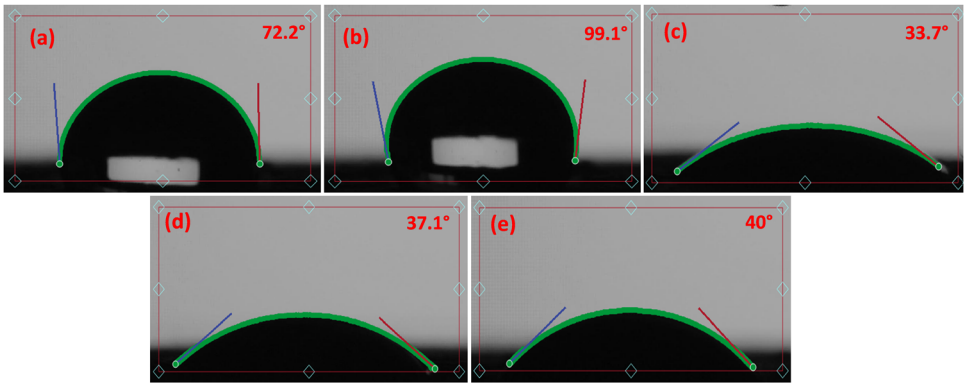

Fig. 8 Contact angle measurements for (a) IHSC, (b) IHSC-900, (c) Ce-IHSC-700, (d) Ce-IHSC-800, and (e) Ce-IHSC-900.

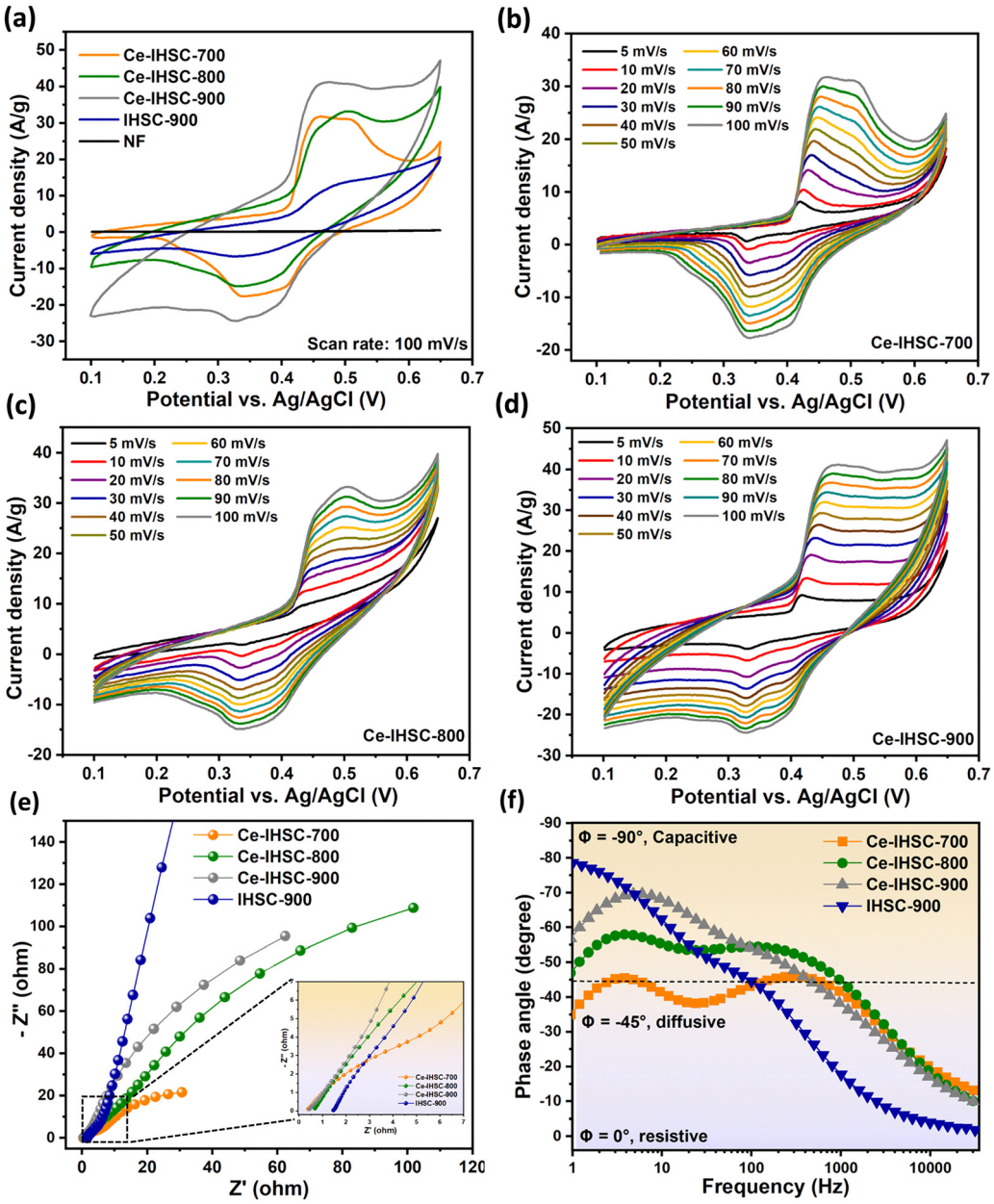

Fig. 9 (a) CV profiles of IHSC-900 and Ce-IHSC-*x* at a constant scan rate of 100 mV s^{-1}; CV profiles of (b) Ce-IHSC-700, (c) Ce-IHSC-800, (d) Ce-IHSC-900 at scan rates from 5 to 100 mV s^{-1}, (e) Nyquist plots for IHSC-900 and Ce-IHSC-*x*; inset depicts the high-frequency intercept of Nyquist plots and (f) bode plots for IHSC-900 and Ce-IHSC-*x*.

cathodic and anodic sides of the CV profile of IHSC-900 represents the redox reactions related to surface oxygen, N functional groups, and Fe-species. In comparison, ceria-modified hydrochars exhibit additional distinct redox features which are mainly contributed by the faradaic redox reactions governed by Ce in ceria nanoparticles as follows:[47]

$$Ce^{IV}O_2 + OH^- \leftrightarrow Ce^{III}O_2OH + e^- \quad (2)$$

Besides the redox reactions, carbon materials especially with enriched microposrosity also contribute to charge storage through the accumulation of ions at electrode/electrolyte interface through the development of an electrical double layer (EDL).[48] Notably, the integral CV area of Ce-IHSC-*x* is significantly larger compared to IHSC-900. For Ce-IHSC-*x*, the CV area progressively increases with the rise in post-heat treatment temperature from 700 to 900 °C. These results clearly show that the incorporation of ceria and post-heat treatment temperature influence the electrochemical performance of hydrochars. Among all samples, Ce-IHSC-900 revealed the highest electrochemical activity in terms of integrated CV area as well as the magnitude of current density, which is attributed to its unique structure, interstitial porosity, and composition. Furthermore, the CV measurements at various scan rates in

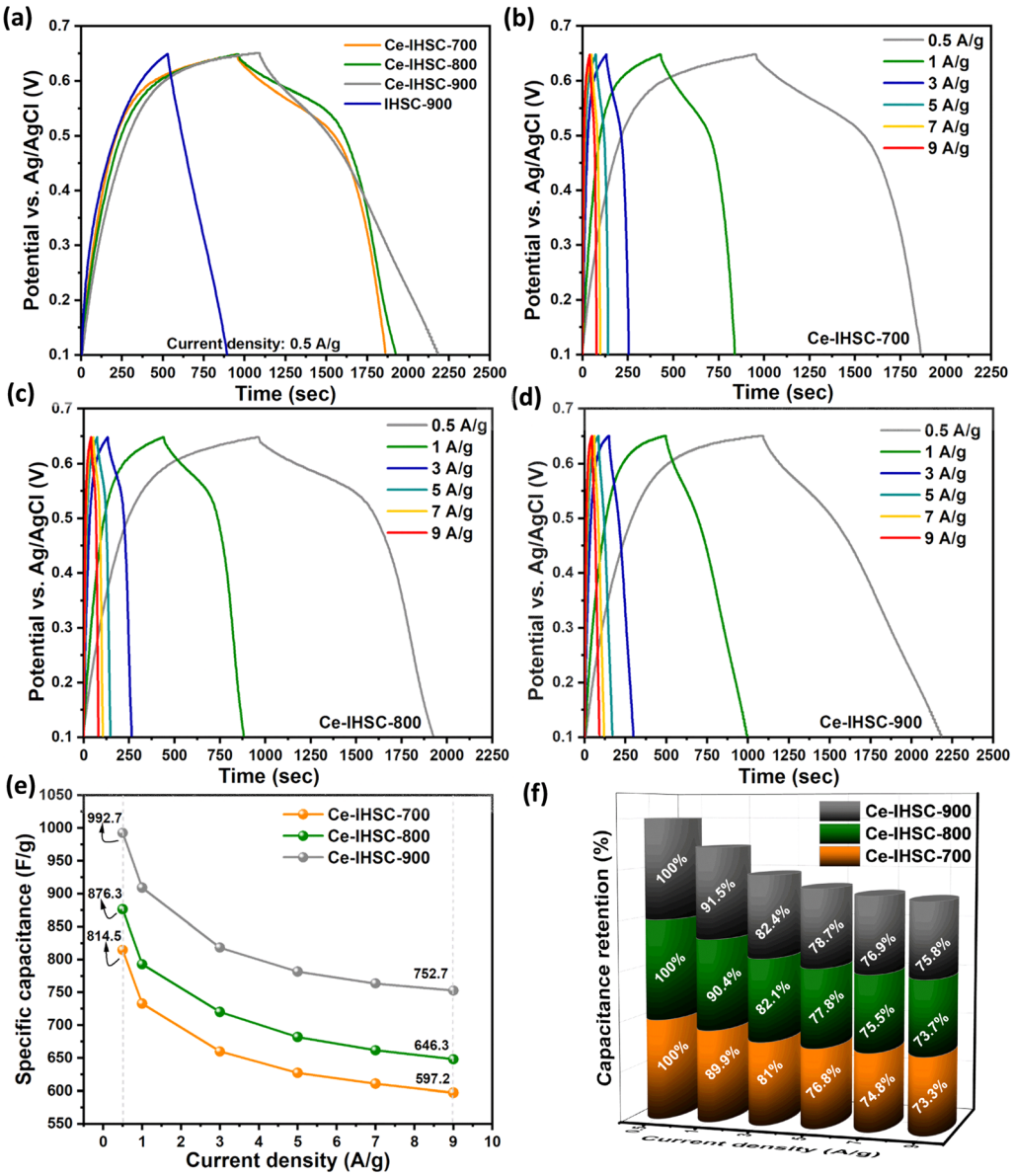

Fig. 10 (a) GCD plots of IHSC-900 and Ce-IHSC-*x* at a current density of 0.5 A g^{-1}; GCD plots of (b) Ce-IHSC-700, (c) Ce-IHSC-800, and (d) Ce-IHSC-900 at current densities from 0.5 to 9 A g^{-1}, (e) trend of specific capacitance *vs.* applied current density, and (f) capacitance retention *vs.* applied current density.

Fig. 9(b–d) show that Ce-IHSC-*x* maintain their typical CV signatures at all scan rates, suggesting high rate capability. Nonetheless, the redox peaks shift slightly toward the anodic and cathodic ends with increased scan rate, due to kinetic limitations and ohmic resistance at higher rates, causing minor deviations from the equilibrium potential.[49]

Electrochemical impedance analysis was employed to investigate the impedance characteristics of hydrochars in contact with electrolytes by measuring their frequency-dependent response. The resulting Nyquist plots shown in Fig. 9(e) provide valuable insights into the electrochemical processes that govern the movement of electrons and ions at electrode/electrolyte interface. The intercept of Nyquist at the high frequency shows equivalent series resistance (ESR) which is comprised of the resistance from active material, electrolyte, and contact resistance at electrode/electrolyte interface.[50] The value of ESR for IHSC-900, Ce-IHSC-700, Ce-IHSC-800, and Ce-IHSC-900 is found to be 1.47, 0.40, 0.57, and 0.51 Ω, respectively. The decrease in ESR of ceria-modified hydrochars as compared to IHSC-900 is attributed to the increased wettability of electrodes and the formation of conductive electron pathways among ceria nanoparticles and conductive carbon domains. Still, the slightly higher value of ESR for hydrochars pyrolyzed at higher temperature can be attributed to the hydrophobic surface which influences the contact resistance at the electrode/electrolyte interface. Similar observations were made previously for agro-waste derived biochar with different carbonization temperature.[51] The distorted semicircles at high frequencies

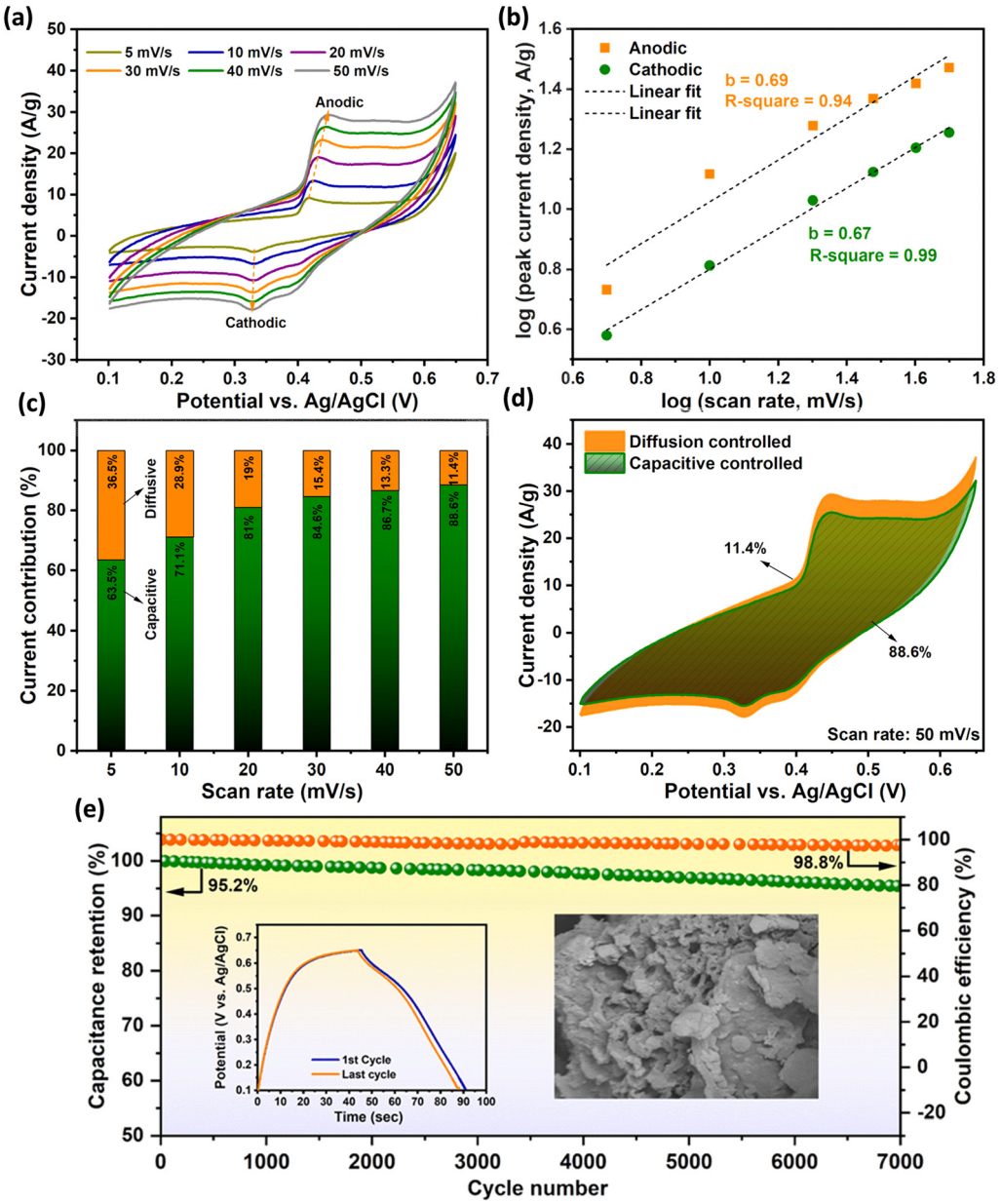

Fig. 11 (a) CV profiles of Ce-IHSC-900 at scan rates from 5 to 50 mV s^{-1}, (b) plot showing log (scan rate) *vs.* log (peak current density), (c) current contribution from diffusion and capacitive processes at different applied scan rates, (d) CV profile showing deconvoluted diffusion and capacitive contribution at 50 mV s^{-1}, and (e) cyclic stability plot of Ce-IHSC-900 measured at 9 A g^{-1}.

arise from complex charge transfer pathways, characteristic of highly porous materials with combined bulk, pore, and surface effects.[52] Extrapolating the vertical line at low frequency yields the charge transfer resistance (R_{CT}). Notably, Ce-IHSC-900 presented a low value of R_{CT} (0.94 Ω) as compared to Ce-IHSC-700 (2.06 Ω), Ce-IHSC-800 (1.22 Ω), and IHSC-900 (3.19 Ω) due to its low charge transfer resistance. Reduction in R_{CT} for Ce-IHSC-900 can be attributed to its improved electrical conductivity resulting from increased graphenization, and its larger crystallite size with fewer grain boundaries which minimizes charge carrier scattering and enhances charge transfer kinetics. Other than this, bode plots in Fig. 9(f) reveal the impedance phase angle *vs.* frequency obtained from the EIS analysis. The phase angle for IHSC-900 (79°) at low frequency is close to 90° indicating its predominant capacitive behavior, whereas the phase angles for Ce-IHSC-*x i.e.*, 34.8°, 47.1°, and 56.7° in line with the post heat treatment temperature are far from the ideal capacitor, which indicates the inclusion of pseudocapacitance.

Supercapacitor performance of hydrochars was further evaluated by the galvanostatic charge–discharge measurements within a potential range of 0.1 to 0.65 V. As shown in Fig. 10(a), pristine IHSC-900 exhibits a quasi-triangular charge–discharge curve. Meanwhile, Ce-IHSC-*x* shows diffused plateaus along charge–discharge plots due to the charge storage

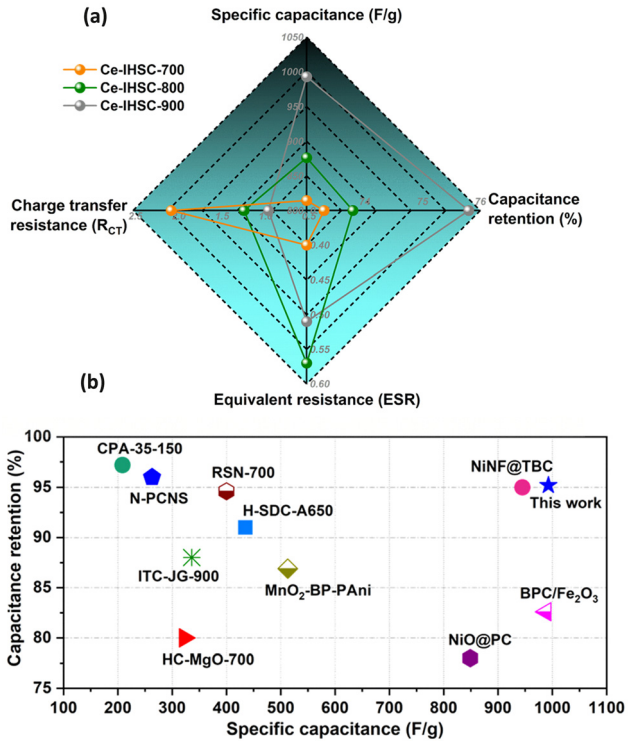

Fig. 12 (a) Radar plot showing a comparison of electrochemical performance parameters for Ce-IHSC-700, Ce-IHSC-800, and Ce-IHSC-900, (b) plots showing a comparison of specific capacitance and cyclic stability of Ce-IHSC-900 with similar reported biomass-derived carbon materials.

from combined EDL and faradaic reactions. The quasi-symmetric charge–discharge curves for all hydrochars imply good coulombic efficiency. The initial coulombic efficiency for IHSC-900, Ce-IHSC-700, Ce-IHSC-800, Ce-IHSC-900 was calculated as 100%, 96.8%, 99.3%, and 99.7%, respectively. It is evident from Fig. 10(a) that Ce-IHSC-900 demonstrates the longest charge–discharge time among all hydrochars at a constant current density of 0.5 A g^{-1}, which highlights its superior charge storage capability, which is consistent with the CV measurements. The specific capacitance (C_{sp}) of all electrodes was calculated from the charge–discharge measurements by the following equation:

$$C_{sp} = I \times \Delta t/m \times \Delta V \quad (3)$$

In the above equation, I represent the current, m is the mass of the hydrochar, Δt denotes the discharge time, and ΔV is the applied voltage excluding the ohmic drop. For ceria-modified hydrochars, the specific capacitance is lowest for Ce-IHSC-700 *i.e.*, 814.5 F g^{-1} at 0.5 A g^{-1}. It improves with an increase in post-heat treatment temperature, reaching 876.3 F g^{-1} for Ce-IHSC-800, and achieves the highest value of 992.7 F g^{-1} for Ce-IHSC-900. In the interim, the specific capacitance of IHSC-900 is calculated as 325.4 F g^{-1} which is significantly lower than that of Ce-IHSC-900 (992.7 F g^{-1}). The three-fold enhancement in specific capacitance of Ce-IHSC-900 as compared to IHSC-900 is principally rooted in the incorporation of ceria nanoparticles and its hierarchical porosity which significantly activates the hydrochar for charge storage. Apart from this, to specifically observe the effect of the IL on the electrochemical performance of the electrodes, a comparative electrochemical study was conducted on ceria-modified hydrochar prepared under the same hydrothermal conditions in the absence of [Bmim][$FeCl_4$] and heat-treated at 900 °C, as presented in Fig. S8(a–d) (ESI†). The ceria-modified hydrochar synthesized without IL exhibited a similar electrochemical signature in CV, GCD, and EIS analyses, likely due to the predominant redox activity of CeO_2. However, its specific capacitance was 722.7 F g^{-1} at 0.5 A g^{-1}, which is lower than that of the ceria-modified hydrochars prepared in the presence of IL. This difference in electrochemical performance highlights the role of IL in enhancing the capacitance and overall electrochemical behavior of the hydrochar. The effect of applied current density on the charge–discharge characteristic of hydrochars was also investigated. Fig. 10(b–d) displays almost uniform charge–discharge curves of Ce-IHSC-x at all current densities (0.5–9 A g^{-1}). The trend in specific capacitance with applied current density is shown in Fig. 10(e and f). As a general phenomenon, the specific capacitance declines with the increase in current density due to limited mass transport and increased internal resistance of material at high current densities. That being said, Ce-IHSC-700, Ce-IHSC-800, Ce-IHSC-900, managed to retain 73.3% (597.2 F g^{-1}), 73.7% (646.3 F g^{-1}), and 75.8% (752.7 F g^{-1}) of specific capacitance at even a very high current density of 9 A g^{-1}. Whereas, ceria modified hydrochar prepared without IL displayed 67.9% capacitance retention (490.9 F g^{-1}) at 9 A g^{-1}.

The high rate performance of Ce-IHSC-900 can be attributed to its mesopore-rich structure and high degree of graphenization, which propose improved ionic and electronic conductivity, facilitating high charge storage even at amplified current densities.[53] Besides, the insight of charge storage mechanism was acquired for the best performing hydrochar electrode *i.e.*, Ce-IHSC-900 from CV measurements (Fig. 11(a)) by applying the power law generalized in the following equation:[54]

$$\log(i) = b\log(v) + \log(a) \quad (4)$$

Fig. 11(b) displays the dependence of peak current 'i' on scan rate 'v' according to eqn (4). The value of kinetic constant 'b' for the anodic and cathodic current was obtained as 0.69 and 0.67, respectively. The existence of this value of the kinetic constant in the transitional area (between 0.5 to 1) confirms that total charge storage in Ce-IHSC-900 is contributed by both diffusion-controlled faradaic reactions and surface-limited capacitive processes (*i.e.*, EDL). The percentage of current contributions from each process at a specific scan rate was further assessed by the Dunn's equation:[55]

$$i(v) = k_1 v + k_2 v^{1/2} = i_{cap} + i_{diff} \quad (5)$$

The corresponding current contribution percentages from capacitive ($k_1 v$) and diffusion-controlled ($k_2 v^{1/2}$) processes are shown in Fig. 11(c). At a low scan rate of 5 mV s^{-1},

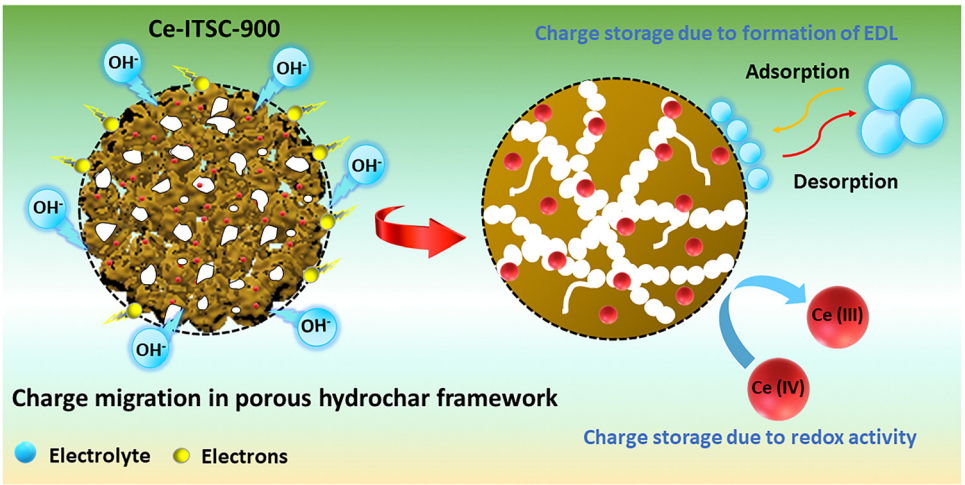

Fig. 13 Schematic illustration of charge storage and facile transport of electrolyte ions and electrons in the 3D channels of porous Ce-IHSC-900 framework.

diffusion-controlled processes contribute 36.5% to charge storage. However, this contribution decreases with increasing scan rate, reaching a minimum of 11.4% at 50 mV s^{-1} (Fig. 11(d)). In addition to the remarkable capacitance performance, the cyclic stability of Ce-IHSC-900 was evaluated by the continuous charge–discharge measurements at 9 A g^{-1} for 7000 cycles and depicted in Fig. 11(e). Ce-IHSC-900 exhibited impressive cyclic stability with 95.2% and 98.8% retention of initial specific capacitance and coulombic efficiency, respectively.

To this end, the electrochemical measurements demonstrate that among the synthesized hydrochars, Ce-IHSC-900 exhibited overall superior performance (see the radar plot in Fig. 12(a)), achieving a high specific capacitance of 992.7 F g^{-1} at 0.5 A g^{-1}, which remained as high as 752.7 F g^{-1} even at 9 A g^{-1}. Nonetheless, the electrochemical performance of Ce-IHSC-900 was benchmarked against similarly reported biomass-derived supercapacitor electrodes (summarized in Fig. 12(b) and Table S2, ESI†). The synthesized spruce cone-derived ceria-modified hydrochar (Ce-IHSC-900) demonstrated comparable or superior specific capacitance and cyclic stability compared to most electrode materials.

The high electrochemical activity of Ce-IHSC-900 can be attributed to several factors, including the abundant carbon interface, enormous active sites provided by CeO_2, high electrical conductivity of N-doped carbon, as well as its favorable morphology and hierarchical porous characteristics (Fig. 13). Additionally, redox-active centers from N-functional groups (pyridinic-N, pyrrolic-N, and graphitic-N) and Fe-species identified through XPS contribute further provide active sites for reactions.[28] Also, as observed from EDX weight percentage (Wt%) analysis, Ce-IHSC-900 exhibited a higher Fe and N content compared to its counterparts treated at lower temperatures. This increased Fe and N incorporation provided additional active sites in Ce-IHSC-900 for improved pseudocapacitance. While specific surface area often influences electrochemical performance, notably, in our case, the performance does not directly correlate with surface area. It has been reported that mesopores, despite sacrificing surface area, enhance ion mobility to active sites and enable more effective utilization of the available surface.[56] Ce-IHSC-900, with its higher contribution of mesoporous surface area as compared to Ce-IHSC-800 and Ce-IHSC-700 (Table 1), supports superior ionic transport and electrolyte accessibility to active sites. Lastly, the optimized post-heat treatment temperature further enhances its properties, such as electrical conductivity, through a higher degree of graphenization, further boosting its electrochemical activity.

4. Conclusions

In summary, ceria-modified and heteroatom-functionalized hydrochar materials (Ce-IHSC-*x*) were successfully synthesized through ionic liquid assisted hydrothermal carbonization of spruce cone biowaste. The resulting hydrochar materials exhibited a high specific surface area (up to 632 m^2 g^{-1}), advantageous porous architecture, and abundant active sites derived from Ce, N, and Fe, making them highly suitable for electrochemical applications. The unique structure and composition of these biomass-derived carbon materials especially those of Ce-IHSC-*x*, endow them with excellent charge storage capacity and long-term stability. Electrodes fabricated using Ce-IHSC-900 demonstrated superior specific capacitance of 992.7 F g^{-1} at 0.5 A g^{-1} and 752.7 F g^{-1} at 9 A g^{-1}, surpassing other Ce-IHSC-*x* electrodes. This high charge storing capacity along with exceptional cyclic stability of 95.2% in terms of capacitance retention, highlights its robustness and potential for supercapacitor applications. This wet-pyrolysis synthesis strategy, along with the precise tuning of active sites, can be extended to other biowaste sources, paving the way for their utilization in diverse electrochemical energy storage technologies.

Data availability

All data generated or analyzed during this study are included in the main article and electronic ESI.†

Conflicts of interest

There are no conflicts to declare.

Acknowledgements

Prof. Zulfiqar is highly thankful for the support provided by the Statutory City of Ostrava, Czechia, through the Research Grant "Global Experts". Prof. Cochran is thankful to the National Science Foundation for financial support through research grants NSF-2113695, NSF-2132200 and NSF-2242763. H. S. acknowledges the Czech Science Foundation (GACR), project 22-23407S, and the Ministry of Education, Youth and Sports of the Czech Republic (MEYS) through V4-Japan joint research program, project 8F21010. The authors would like to thank Prof. Václav Slovák for his efforts in collecting the spruce cones for this project.

References

1 M. Vijayakumar, *et al.*, Conversion of biomass waste into high performance supercapacitor electrodes for real-time supercapacitor applications, *ACS Sustainable Chem. Eng.*, 2019, **7**(20), 17175–17185.
2 L. Guan, *et al.*, Synthesis of biomass-derived nitrogen-doped porous carbon nanosheests for high-performance supercapacitors, *ACS Sustainable Chem. Eng.*, 2019, **7**(9), 8405–8412.
3 C. Zheng, *et al.*, Biomass-based carbon nanofibers modified with polyaniline for supercapacitor applications, *ACS Appl. Nano Mater.*, 2023, **6**(15), 14136–14150.
4 A. P. Khedulkar, *et al.*, Flower-like nickel hydroxide@ tea leaf-derived biochar composite for high-performance supercapacitor application, *J. Colloid Interface Sci.*, 2022, **623**, 845–855.
5 C. Yan, *et al.*, N self-doped multifunctional chitosan biochar-based microsphere with heterogeneous interfaces for self-powered supercapacitors to drive overall water splitting, *Biochar*, 2023, **5**(1), 90.
6 H. Zeng, *et al.*, Insight into the microstructural evolution of anthracite during carbonization-graphitization process from the perspective of materialization, *Int. J. Min. Sci. Technol.*, 2022, **32**(6), 1397–1406.
7 X. Li, L. Colombo and R. S. Ruoff, Synthesis of graphene films on copper foils by chemical vapor deposition, *Adv. Mater.*, 2016, **28**(29), 6247–6252.
8 S. Yuan, *et al.*, Nitrogen conversion during rapid pyrolysis of coal and petroleum coke in a high-frequency furnace, *Appl. Energy*, 2012, **92**, 854–859.
9 Y. Yin, *et al.*, Recent progress and future directions of biomass-derived hierarchical porous carbon: designing, preparation, and supercapacitor applications, *Energy Fuels*, 2023, **37**(5), 3523–3554.
10 M. S. Sayed, *et al.*, Unravelling the role of pore structure of biomass-derived porous carbon in charge storage mechanisms for supercapacitors, *RSC Adv.*, 2024, **14**(34), 24631–24642.
11 S. Aldroubi, *et al.*, Ionothermal Carbonization of Sugarcane Bagasse in 1-Alkyl-3-methylimidazolium Ionic Liquids: Insights into the Role of the Chloroferrate Anion, *J. Phys. Chem. B*, 2024, **128**(14), 3485–3498.
12 K. Xia, *et al.*, Hierarchical porous carbons with controlled micropores and mesopores for supercapacitor electrode materials, *Carbon*, 2008, **46**(13), 1718–1726.
13 W. Ma, *et al.*, Bottom-up fabrication of activated carbon fiber for all-solid-state supercapacitor with excellent electrochemical performance, *ACS Appl. Mater. Interfaces*, 2016, **8**(23), 14622–14627.
14 Y. Fan, *et al.*, Microporous carbon derived from acacia gum with tuned porosity for high-performance electrochemical capacitors, *Int. J. Hydrogen Energy*, 2015, **40**(18), 6188–6196.
15 Y. Liang, R. Fu and D. Wu, Reactive template-induced self-assembly to ordered mesoporous polymeric and carbonaceous materials, *ACS Nano*, 2013, **7**(2), 1748–1754.
16 M. Prieto, *et al.*, Hydrothermal Carbonization of Biomass for Electrochemical Energy Storage: Parameters, Mechanisms, Electrochemical Performance, and the Incorporation of Transition Metal Dichalcogenide Nanoparticles, *Polymers*, 2024, **16**(18), 2633.
17 K. MacDermid-Watts, *et al.*, Effects of $FeCl_3$ catalytic hydrothermal carbonization on chemical activation of corn wet distillers' fiber, *ACS Omega*, 2021, **6**(23), 14875–14886.
18 P. M. Yeletsky, M. V. Lebedeva and V. A. Yakovlev, Today's progress in the synthesis of porous carbons from biomass and their application for organic electrolyte and ionic liquid based supercapacitors, *J. Energy Storage*, 2022, **50**, 104225.
19 L. Cibien, *et al.*, Ionothermal carbonization in [Bmim][$FeCl_4$]: an opportunity for the valorization of raw lignocellulosic agrowastes into advanced porous carbons for CO_2 capture, *Green Chem.*, 2020, **22**(16), 5423–5436.
20 Y. Liu, *et al.*, Biomass-derived hierarchical porous carbons: boosting the energy density of supercapacitors via an ionothermal approach, *J. Mater. Chem. A*, 2017, **5**(25), 13009–13018.
21 P. Zhang, *et al.*, Updating biomass into functional carbon material in ionothermal manner, *ACS Appl. Mater. Interfaces*, 2014, **6**(15), 12515–12522.
22 L.-L. Ma, *et al.*, Ionothermal carbonization of biomass to construct sp^2/sp^3 carbon interface in N-doped biochar as efficient oxygen reduction electrocatalysts, *Chem. Eng. J.*, 2020, **400**, 125969.
23 M. Baccour, *et al.*, Carbonization of polysaccharides in $FeCl_3$/BmimCl ionic liquids: Breaking the capacity barrier of carbon negative electrodes in lithium ion batteries, *J. Power Sources*, 2020, **474**, 228575.
24 A. Joseph, S. Perikkathra and T. Thomas, Novel 2D CeO_2 nanoflakes as a high-performance asymmetric supercapacitor electrode material, *J. Energy Storage*, 2023, **68**, 107757.
25 P. Periasamy, *et al.*, Breaking Barriers of CeO_2 in Energy Storage: Hydrothermal Energized Preparation of Mesoporous Carbon Added CeO_2 Nanohybrids as Supercapacitor Electrodes, *Electrochim. Acta*, 2024, 145144.

26 A. Sadezky, *et al.*, Raman microspectroscopy of soot and related carbonaceous materials: Spectral analysis and structural information, *Carbon*, 2005, **43**(8), 1731–1742.
27 M. Thommes, *et al.*, Physisorption of gases, with special reference to the evaluation of surface area and pore size distribution (IUPAC Technical Report), *Pure Appl. Chem.*, 2015, **87**(9–10), 1051–1069.
28 H.-C. Li, *et al.*, Ionothermal carbonization of biomass to construct Fe, N-doped biochar with prominent activity and recyclability as cathodic catalysts in heterogeneous electro-Fenton, *ACS ES&T Eng.*, 2020, **1**(1), 21–31.
29 X. Ju, *et al.*, An improved X-ray diffraction method for cellulose crystallinity measurement, *Carbohydr. Polym.*, 2015, **123**, 476–481.
30 Y. Niu, *et al.*, Synthesis of N-doped carbon with embedded Fe/Fe_3C particles for microwave absorption, *J. Mater. Sci.*, 2020, **55**, 11970–11983.
31 F. I. Saaid, *et al.*, The synergistic effect of iron cobaltite compare to its single oxides as cathode in supercapacitor, *J. Electroceram.*, 2020, **44**, 183–194.
32 Z.-L. Xie, *et al.*, Hierarchical porous carbonaceous materials via ionothermal carbonization of carbohydrates, *J. Mater. Chem.*, 2011, **21**(20), 7434–7442.
33 U. P. Agarwal, Analysis of cellulose and lignocellulose materials by Raman spectroscopy: a review of the current status, *Molecules*, 2019, **24**(9), 1659.
34 S. Aldroubi, *et al.*, Ionothermal carbonization of sugarcane bagasse in imidazolium tetrachloroferrate ionic liquids: effect of the cation on textural and morphological properties, *Green Chem.*, 2023, **25**(9), 3533–3542.
35 H. Tonnoir, *et al.*, Pyrolysis temperature dependence of sodium storage mechanism in non-graphitizing carbons, *Carbon*, 2023, **208**, 216–226.
36 K. Maliutina, A. Tahmasebi and J. Yu, Effects of pressure on morphology and structure of bio-char from pressurized entrained-flow pyrolysis of microalgae, *Data in brief*, 2018, **18**, 422–431.
37 C. P. Supriadi, *et al.*, Synthesis and characterization of carbon material obtained from coconut coir dust by hydrothermal and pyrolytic processes, *Int. J. Technol.*, 2017, **8**(8), 1470–1478.
38 O. Farobie, *et al.*, In-depth study of bio-oil and biochar production from macroalgae Sargassum sp. via slow pyrolysis., *RSC Adv.*, 2022, **12**(16), 9567–9578.
39 A. Iaccarino, R. Gautam and S. M. Sarathy, Bio-oil and biochar production from halophyte biomass: effects of pre-treatment and temperature on Salicornia bigelovii pyrolysis, *Sustainable Energy Fuels*, 2021, **5**(8), 2234–2248.
40 H. Chen, *et al.*, Preparation of pickling-reheating activated alfalfa biochar with high adsorption efficiency for p-nitrophenol: characterization, adsorption behavior, and mechanism, *Environ. Sci. Pollut. Res.*, 2019, **26**, 15300–15313.
41 J. Gao, *et al.*, Construction of a sp^3/sp^2 carbon interface in 3D N-doped nanocarbons for the oxygen reduction reaction, *Angew. Chem., Int. Ed.*, 2019, **58**(42), 15089–15097.
42 Z. Lin, *et al.*, Facile synthesis of nitrogen-doped graphene via pyrolysis of graphene oxide and urea, and its electrocatalytic activity toward the oxygen-reduction reaction, *Adv. Energy Mater.*, 2012, **2**(7), 884–888.
43 J. Xiao, *et al.*, Ultra-small Fe2N nanocrystals embedded into mesoporous nitrogen-doped graphitic carbon spheres as a highly active, stable, and methanol-tolerant electrocatalyst for the oxygen reduction reaction, *Nano Energy*, 2016, **24**, 121–129.
44 W. Niu, *et al.*, Mesoporous N-doped carbons prepared with thermally removable nanoparticle templates: an efficient electrocatalyst for oxygen reduction reaction, *J. Am. Chem. Soc.*, 2015, **137**(16), 5555–5562.
45 W. Weng, *et al.*, Thermoelectrochemical formation of Fe/Fe3C@ hollow N-doped carbon in molten salts for enhanced catalysis, *J. Mater. Chem. A*, 2020, **8**(9), 4800–4806.
46 Z. Wang, *et al.*, Formation, detection, and function of oxygen vacancy in metal oxides for solar energy conversion, *Adv. Funct. Mater.*, 2022, **32**(7), 2109503.
47 D. Deng, *et al.*, Electrochemical performance of CeO_2 nanoparticle-decorated graphene oxide as an electrode material for supercapacitor., *Ionics*, 2017, **23**, 121–129.
48 T. Li, *et al.*, The synthesis and performance analysis of various biomass-based carbon materials for electric double-layer capacitors: a review, *Int. J. Energy Res.*, 2020, **44**(4), 2426–2454.
49 Y. Sun, *et al.*, Biomass-derived carbon for high-performance batteries: from structure to properties, *Adv. Funct. Mater.*, 2022, **32**(24), 2201584.
50 A. A. Mohammed, *et al.*, Flexible asymmetric supercapacitor based on Hyphaene fruit shell-derived multi-heteroatom doped carbon and $NiMoO_4$@ $NiCo_2O_4$ hybrid structure electrodes., *Biomass Bioenergy*, 2023, **179**, 106981.
51 Z. Husain, *et al.*, Nano-sized mesoporous biochar derived from biomass pyrolysis as electrochemical energy storage supercapacitor, *Mater. Sci. Energy Technol.*, 2022, **5**, 99–109.
52 P. Makkar, A. Malik and N. N. Ghosh, Biomass-derived porous carbon-anchoring $MnFe_2O_4$ hollow sphere and needle-like NiS for a flexible all-solid-state asymmetric supercapacitor, *ACS Appl. Energy Mater.*, 2021, **4**(6), 6015–6024.
53 X. Yuan, *et al.*, Tunable synthesis of biomass-based hierarchical porous carbon scaffold@ MnO_2 nanohybrids for asymmetric supercapacitor., *Chem. Eng. J.*, 2020, **393**, 121214.
54 M. Zhang, *et al.*, Biomass-derived graphitic carbon/Co_3O_4 nanocomposites with pseudocapacitance for lithium storage., *ACS Appl. Nano Mater.*, 2021, **4**(2), 1340–1350.
55 S. S. Gunasekaran, *et al.*, Phytogenic generation of NiO nanoparticles as green-electrode material for high performance asymmetric supercapacitor applications, *J. Energy Storage*, 2021, **37**, 102412.
56 Y. Lin, *et al.*, Multifunctional template prepares N-, O-, and S-codoped mesoporous 3D hollow nanocage biochar with a multilayer wall structure for aqueous high-performance supercapacitors, *ACS Appl. Energy Mater.*, 2023, **6**(4), 2265–2275.